Journal of Computational Physics 230 (2011) 2806–2820

Contents lists available at ScienceDirect

Journal of Computational Physics

journal homepage: www.elsevier.com/locate/jcp

Numerical wave propagation for the triangular $P1_{DG}$–$P2$ finite element pair

C.J. Cotter [a,*], D.A. Ham [b,c]

[a] Department of Aeronautics, Imperial College London, South Kensington Campus, London SW7 2AZ, United Kingdom
[b] Department of Earth Science and Engineering, Imperial College London, South Kensington Campus, London SW7 2AZ, United Kingdom
[c] Grantham Insitute for Climate Change, Imperial College London, South Kensington Campus, London SW7 2AZ, United Kingdom

ARTICLE INFO

Article history:
Received 26 July 2010
Received in revised form 14 October 2010
Accepted 16 December 2010
Available online 24 December 2010

Keywords:
Mixed finite elements
Geophysical fluid dynamics
Rossby waves
Spurious modes
Numerical weather prediction

ABSTRACT

The f-plane and β-plane wave propagation properties are examined for discretisations of the linearised rotating shallow-water equations using the $P1_{DG}$–$P2$ finite element pair on arbitrary triangulations in planar geometry. A discrete Helmholtz decomposition of the functions in the velocity space based on potentials taken from the pressure space is used to provide a complete description of the numerical wave propagation for the discretised equations. In the f-plane (planar geometry, Coriolis force independent of space) case, this decomposition is used to obtain decoupled equations for the geostrophic modes, the inertia-gravity modes, and the inertial oscillations. As has been noticed previously, the geostrophic modes are steady. The Helmholtz decomposition is used to show that the resulting inertia-gravity wave equation is third-order accurate in space. In general the $P1_{DG}$–$P2$ finite element pair is second-order accurate, so this leads to very accurate wave propagation. It is further shown that the only spurious modes supported by this discretisation are spurious inertial oscillations which have frequency f, and which do not propagate. A restriction of the $P1_{DG}$ velocity space is proposed in which these modes are not present, leading to a finite element discretisation which is completely free of spurious modes. The Helmholtz decomposition also allows a simple derivation of the quasi-geostrophic limit of the discretised $P1_{DG}$–$P2$ equations in the β-plane (planar geometry, Coriolis force linear in space) case resulting in a Rossby wave equation which is also third-order accurate. This means that the dispersion relation for the wave propagation is very accurate; an illustration of this is provided by a numerical dispersion analysis in the case of a triangulation consisting of equilateral triangles.

1. Introduction

Recently there has been growing interest in developing more general horizontal discretisation schemes for numerical weather prediction (NWP) models with computational meshes constructed from triangles or hexagons. There are two principal motivations for this. Firstly, geodesic grids (which are obtained by iterative refinement of an icosahedron using triangles, sometimes transforming to the dual grid which is a mesh of hexagons with exactly 12 pentagons located at the vertices of the original icosahedron) provide similar grid cell areas over the entire sphere, which has possible advantages for accurate representation of wave propagation. Furthermore, geodesic grids also avoid the very fine grid cells obtained near the North and South poles on latitude–longitude grids, which lead to large Courant numbers, and cause bottlenecks in communication between processors on parallel systems. This has led to a number of groups developing weather and climate models which use geodesic grids [14,11,17]. Secondly, triangles facilitate the implementation of adaptive mesh refinement. This allows nested regional models

* Corresponding author.
E-mail address: colin.cotter@imperial.ac.uk (C.J. Cotter).

0021-9991/$ - see front matter © 2010 Elsevier Inc. All rights reserved.
doi:10.1016/j.jcp.2010.12.024

within a global model, and further allows dynamic mesh refinement in which the mesh resolution is locally modified in response to the dynamics in the course of a forecast. The development of new numerical schemes that correctly represent the qualitative properties of wave propagation on these grids, and under adaptive-mesh refinement, is crucial.

Possible discretisations on triangular or hexagonal meshes are obtained using three different approaches: finite difference methods, finite volume methods and finite element methods. To eliminate spurious pressure modes, finite difference methods use a C-grid in which the edge-normal velocity is stored at the edge-centres, and the pressure is stored at the cell-centres. On quadrilateral grids, the wave propagation is observed to be well represented provided that the Rossby radius is well-resolved [1,6,12]. On triangular and hexagonal grids the problem lies in finding a scheme for reconstructing the Coriolis force (which requires the tangential velocity) from the normal velocity. Recently, a reconstruction scheme was found which results in steady geostrophic modes for C-grid discretisations on the regular hexagonal grid in the plane [19]. In the same paper it was shown that the resulting discrete system on the β-plane has a spurious extra Rossby wave branch, with very slow Eastward phase velocities. This reconstruction was extended to arbitrarily structured C-grids in Thuburn et al. [20]. The finite element method provides a great degree of flexibility in the choices of discretisation for velocity and pressure. Amongst the many finite element pairs that have been proposed for the rotating shallow-water equations are the $P1_{NC}$–$P1$ and $P1$–iso $P2$–$P1$ elements (investigated and compared to several other element pairs in Le Roux et al. [10]), the RT0 elements (introduced in Raviart [13] and proposed for the shallow-water equations in Walters and Casulli [22]) and equal-order elements with stabilisation (also proposed in Walters and Casulli [22]).

In this paper we study the wave propagation properties of the recently proposed $P1_{DG}$–$P2$ finite element discretisation. The $P1_{DG}$–$P2$ finite element discretisation was introduced in Cotter et al. [5], and was designed to accommodate the geostrophic balance relation between pressure and velocity without introducing spurious pressure modes. This is achieved by using a quadratic ($P2$) continuous finite element basis for pressure, and a linear discontinuous ($P1_{DG}$) finite element basis for velocity (hence the name $P1_{DG}$–$P2$). The pressure polynomials are one order higher than the velocity polynomials, which accommodates the geostrophic balance relation since the pressure gradient and the velocity are both linear within each element. Making the velocity basis discontinuous increases the number of velocity degrees of freedom so that there are no spurious pressure modes. The lack of pressure modes was investigated numerically in Cotter et al. [5] and subsequently proved in Cotter et al. [4], where it was also shown that this combination of spaces means that geostrophically balanced states are exact steady states of the linear equations on arbitrary unstructured meshes (this property can also be obtained for C-grid finite difference methods as described in Thuburn et al. [20], with the added restriction that the meshes satisfy an orthogonality property). In this paper we go further and produce a complete description of the numerical wave propagation properties of $P1_{DG}$–$P2$, which is facilitated by the construction of a discrete Helmholtz decomposition of the $P1_{DG}$ space.

The rest of this paper is organised as follows. In Section 2, we show that $P1_{DG}$–$P2$ has a discrete Helmholtz decomposition. In Section 3 we use this decomposition to analyse the wave propagation on the f-plane. We show that there are three types of modes: steady geostrophic modes, inertia–gravity modes, and inertial oscillations (of which only one is a physical mode). We show that the inertial oscillations do not propagate and can be filtered out by solving two discretised elliptic equations. We also show that the velocity may be eliminated to obtain a third-order accurate inertia–gravity wave equation, and hence claim that the wave propagation is very accurate on arbitrary unstructured meshes. In Section 4, we use the Helmholtz decomposition to analyse the Rossby wave propagation on the β-plane in the quasi-geostrophic limit (following the approach of Thuburn [19]). We obtain a third-order accurate Rossby wave equation, and hence claim that the Rossby wave equation is also very accurate. Finally, in Section 5 we give a summary and outlook.

2. Discrete Helmholtz decomposition for $P1_{DG}$–$P2$

In this section we show that the $P1_{DG}$–$P2$ finite element discretisation has a discrete Helmholtz decomposition for $P1_{DG}$–$P2$. We shall adopt the notation that the δ superscript indicates a numerical approximation in a finite element space; functions without subscripts indicate continuous fields. We start by stating two properties of $P1_{DG}$–$P2$ which we shall use throughout.

Definition 1 (*Embedding conditions*). Let V be the chosen vector space of finite element velocity fields (in the case of $P1_{DG}$–$P2$, V is the space $P1_{DG}$ of velocity fields u^δ that are linear in each triangular element, with no continuity constraints across element boundaries), and let H be the chosen vector space of finite element pressure fields (in the case of $P1_{DG}$–$P2$, H is the space $P2$ of pressure fields h^δ that are quadratic in each triangular element and are constrained to be continuous across element boundaries).

1. The operator ∇ defined by the pointwise gradient

$$q^\delta(\boldsymbol{x}) = \nabla h^\delta(\boldsymbol{x})$$

maps from H into V.
2. The skew operator $\perp$ defined by the pointwise formula

$$\boldsymbol{q}^\delta(\boldsymbol{x}) = (\boldsymbol{u}^\delta(\boldsymbol{x}))^\perp = (-u_2^\delta, u_1^\delta)$$

maps from V into itself.

These are the only conditions that we use in the paper and hence any properties extend to any other finite element pair that satisfies these conditions ($P0$–$P1$ or Pn_{DG}–$P(n+1)$ with any $n > 1$, for example).

These conditions are most definitely not satisfied by all possible pairs (V,H), as illustrated by the following examples.

Example 2 (*P1–P1*). The finite element pair known as $P1$–$P1$ (which may be used for the shallow-water equations but requires stabilisation as described in Walters and Casulli [22]) is defined as follows:

- The mesh $\mathcal{M}$ is composed of triangular elements.
- H is the space of elementwise-linear functions h^δ which are continuous across element boundaries.
- V is the space of vector fields u^δ with both of the Cartesian components (u^δ, v^δ) in H.

Condition 1 of Definition 1 is not satisfied by the $P1$–$P1$ pair since gradients of functions in H are discontinuous across element boundaries. Condition 2 is satisfied since the same continuity conditions are required for normal and tangential components.

Example 3 (*RT0*). The lowest order Raviart–Thomas [13] velocity space (known as RT0) is constructed on a mesh $\mathcal{M}$ composed of triangular elements. It consists of elementwise constant vector fields which are constrained to have continuous normal components across element boundaries. RT0 does not satisfy condition 2 of Definition 1 since the $\perp$ operator transforms vector fields with discontinuities in the tangential component (which are permitted in RT0) into vector fields with discontinuities in the normal component (which are not).

We now describe some examples of finite element pairs which *do* satisfy the conditions in Definition 1.

Example 4 (*P0–P1*). The finite element pair known as $P0$–$P1$ (applied to ocean modelling in Umgiesser et al. [21], and analysed in [16,15]) is defined as follows:

- The mesh $\mathcal{M}$ is composed of triangular elements.
- H is the space of elementwise-linear functions h^δ which are continuous across element boundaries.
- V is the space of elementwise-constant vectors with discontinuities across element boundaries permitted.

Example 5 (*$P1_{DG}$–P2*). The finite element pair known as $P1_{DG}$–$P2$ [5] is defined as follows:

- The mesh $\mathcal{M}$ is composed of triangular elements.
- H is the space of elementwise-quadratic functions h^δ which are continuous across element boundaries.
- V is the space of elementwise-linear vectors with discontinuities across element boundaries permitted.

Each of these examples satisfy both conditions in Definition 1: condition 1 holds because taking the gradient of a elementwise polynomial $n+1$ which is continuous across element boundaries results in a vector field which is discontinuous across element boundaries and is composed of elementwise polynomials of degree n, and condition 2 holds since the velocity space uses the same continuity constraints for normal and tangential components i.e. both components are allowed to be discontinuous. This defines a whole sequence of high-order Pn_{DG}–$P(n+1)$ element pairs. Similar elements can be constructed on quadrilateral elements. Since we only require these two conditions to prove our optimal balance property which holds on arbitrary meshes, we can also construct finite element spaces on mixed meshes composed of quadrilaterals and triangles, for example. It is also possible to use p-adaptivity in which different orders of polynomials are used in different elements, as long as the conditions are satisfied. To make the rest of the paper less abstract, we shall only discuss $P1_{DG}$–$P2$, but all of the results are easily extended (with the appropriate orders of accuracy) to any element pair satisfying Definition 1.

Next we note that the gradient of and skew-gradient of any two pressure fields ϕ^δ, ψ^δ in the pressure space $P2$ are orthogonal in the L_2 inner product,

$$\langle \nabla\psi^\delta, \nabla^\perp\phi^\delta\rangle = \int_\Omega \nabla\psi^\delta \cdot \nabla^\perp\phi^\delta \mathrm{d}V = 0,$$

where Ω is the solution domain which is either the sphere, or a domain with periodic boundary conditions. This was proved by direct computation in Cotter et al. [4]. Hence, any velocity field $\boldsymbol{u}^\delta$ in $P1_{DG}$ can be written uniquely in an orthogonal decomposition

$$\boldsymbol{u}^\delta = \bar{\boldsymbol{u}}^\delta + \nabla\phi^\delta + \nabla^\perp\psi^\delta + \hat{\boldsymbol{u}}^\delta, \tag{1}$$

where $\bar{\boldsymbol{u}}^\delta$ is independent of space, where ϕ^δ and ψ^δ are both in the space $\overline{P2}$, which consists of $P2$ functions with mean zero, *i.e.*

$$\langle \phi^\delta, 1\rangle = \int_\Omega \phi^\delta \mathrm{d}V = 0, \quad \langle \psi^\delta, 1\rangle = \int_\Omega \psi^\delta \mathrm{d}V = 0$$

and where $\hat{\boldsymbol{u}}^\delta$ is orthogonal to the gradient or skew-gradient of any $\overline{P2}$ function α^δ, i.e.

$$\langle \hat{\boldsymbol{u}}^\delta, \nabla\alpha^\delta\rangle = \langle \hat{\boldsymbol{u}}^\delta, \nabla^\perp\alpha^\delta\rangle = 0.$$

Furthermore, if any such $\hat{\boldsymbol{u}}^\delta$ satisfies

$$\langle \hat{\boldsymbol{u}}^\delta, \hat{\boldsymbol{u}}^\delta\rangle = 0,$$

then $\hat{\boldsymbol{u}}^\delta = \boldsymbol{0}$, since $\hat{\boldsymbol{u}}^\delta$ is obtained from orthogonal completion. In general the dimension of the orthogonal subspace containing the vector fields of the form $\hat{\boldsymbol{u}}^\delta$ is non-zero, since there are more than twice as many degrees of freedom in the velocity space V as the pressure space H. The dimension of V is $6n_f$ (where n_f is the number of elements), and the dimension of H is $n_v + n_e$ (where n_v is the number of vertices and n_e is the number of edges). For doubly periodic boundary conditions, Euler's polyhedral formula on the torus then gives $\dim(H) = n_v + n_e = 2n_e - n_f$. For a triangulation, $2n_e = 3n_f$ since each triangle has three edges which are each shared between two faces, so $\dim(H) = 2n_f < 3n_f = \dim(V)/2$. Since $2\dim(H) < \dim(V)$ it is not possible to span V entirely with functions of the form $\nabla^\perp\psi^\delta + \nabla\phi^\delta$, ψ^δ, $\phi^\delta \in H$, and so components of the form $\hat{\boldsymbol{u}}^\delta$ will always be present.

Eq. (1) is identical to the Helmholtz decomposition for arbitrary continuous velocity fields in which any continuous velocity field $\boldsymbol{u}$ can be written as a constant plus a gradient of a potential plus the skew gradient of a streamfunction; the only difference in the discrete $P1_{DG}$–$P2$ case is the extra component $\hat{\boldsymbol{u}}^\delta$. This extra component gives rise to spurious inertial oscillations in the $P1_{DG}$–$P2$ finite element discretisation applied to the rotating shallow-water equations. It is possible to describe a reduced velocity space, which we call $H(P2)$, consisting of velocity fields which can be written as

$$\boldsymbol{v}^\delta = \bar{\boldsymbol{v}}^\delta + \nabla\phi^\delta + \nabla^\perp\psi^\delta,$$

where $\bar{\boldsymbol{v}}^\delta$ is independent of space, where ϕ^δ and ψ^δ are both in the space $\overline{P2}$, *i.e.* we have removed the spurious velocity component. It is possible to project a $P1_{DG}$ velocity field $\boldsymbol{u}^\delta$ into $H(P2)$, by first computing the mean component,

$$\bar{\boldsymbol{u}}^\delta = \frac{\int_\Omega \boldsymbol{u}^\delta \mathrm{d}V}{\int_\Omega \mathrm{d}V}$$

and then extracting the velocity potential and streamfunction by solving

$$\langle \nabla\alpha^\delta, \nabla\phi^\delta\rangle = \langle \nabla\alpha^\delta, \boldsymbol{u}^\delta\rangle$$

and

$$\langle \nabla\alpha^\delta, \nabla\psi^\delta\rangle = \langle \nabla^\perp\alpha^\delta, \boldsymbol{u}^\delta\rangle$$

for all $\overline{P2}$ functions α^δ. This amounts to solving elliptic problems for ϕ^δ and ψ^δ. Then, the projection of $\boldsymbol{u}^\delta$ into $H(P2)$ is given by

$$\bar{\boldsymbol{u}}^\delta + \nabla\phi^\delta + \nabla^\perp\psi^\delta.$$

3. Discrete wave propagation on the *f*-plane

In this section we describe all of the numerical solutions obtained from $P1_{DG}$–$P2$ applied to the f-plane.

3.1. Discrete wave equation on the f-plane

The $P1_{DG}$–$P2$ spatial discretisation of the rotating shallow-water equations (see Cotter et al. [4] for a derivation) is

$$\frac{\mathrm{d}}{\mathrm{d}t}\langle \boldsymbol{w}^\delta, \boldsymbol{u}^\delta\rangle + \langle f\boldsymbol{w}^\delta, (\boldsymbol{u}^\delta)^\perp\rangle = -c^2\langle \boldsymbol{w}^\delta, \nabla\eta^\delta\rangle, \tag{2}$$

$$\frac{\mathrm{d}}{\mathrm{d}t}\langle \phi^\delta, \eta^\delta\rangle = \langle \nabla\phi^\delta, \boldsymbol{u}^\delta\rangle, \tag{3}$$

where the velocity $\boldsymbol{u}^\delta$ is in $P1_{DG}$, the layer depth $\eta^\delta = H(1+\eta^\delta)$ is in $P2$, for all test functions $\boldsymbol{w}^\delta$ in $P1_{DG}$ and ϕ^δ in $P2$, and where $c = \sqrt{gH}$ is the non-rotating wave propagation speed, g is the acceleration due to gravity, H is the mean layer depth and f is the Coriolis parameter.

On the f-plane, f is a constant, and so we may take it outside the Coriolis integral. Applying the discrete Helmholtz decomposition to the velocity $\boldsymbol{u}^\delta$ and the velocity test functions $\boldsymbol{w}^\delta$, *i.e.*,

$$\boldsymbol{u}^\delta = \bar{\boldsymbol{u}}^\delta + \nabla\phi^\delta + \nabla^\perp\psi^\delta + \hat{\boldsymbol{u}}^\delta, \quad \boldsymbol{w}^\delta = \bar{\boldsymbol{w}}^\delta + \nabla\alpha^\delta + \nabla^\perp\beta^\delta + \hat{\boldsymbol{w}}^\delta,$$

where α^δ and β^δ are in $P2$.

Eqs. (2) and (3) become (after removing products of orthogonal quantities)

$$\frac{\mathrm{d}}{\mathrm{d}t}\langle\nabla\alpha^\delta,\nabla\phi^\delta\rangle - f\langle\nabla\alpha^\delta,\nabla\psi^\delta\rangle + c^2\langle\nabla\alpha^\delta,\nabla\eta^\delta\rangle = 0, \tag{4}$$

$$\frac{\mathrm{d}}{\mathrm{d}t}\langle\nabla\alpha^\delta,\nabla\psi^\delta\rangle + f\langle\nabla\alpha^\delta,\nabla\phi^\delta\rangle = 0, \tag{5}$$

$$\frac{\mathrm{d}}{\mathrm{d}t}\langle\alpha^\delta,\eta^\delta\rangle - \langle\nabla\alpha^\delta,\nabla\phi^\delta\rangle = 0, \tag{6}$$

$$\frac{\mathrm{d}}{\mathrm{d}t}\langle\bar{\boldsymbol{w}}^\delta,\bar{\boldsymbol{u}}^\delta\rangle + f\langle\bar{\boldsymbol{w}}^\delta,\bar{\boldsymbol{u}}^\delta\rangle = 0, \tag{7}$$

$$\frac{\mathrm{d}}{\mathrm{d}t}\langle\hat{\boldsymbol{w}}^\delta,\hat{\boldsymbol{u}}^\delta\rangle + f\langle\hat{\boldsymbol{w}}^\delta,(\hat{\boldsymbol{u}}^\delta)^\perp\rangle = 0. \tag{8}$$

These solutions exhibit four types of orthogonal modes: geostrophic balance, inertia gravity waves, the physical inertial oscillation, and spurious inertial oscillations due to the presence of $\hat{\boldsymbol{u}}$. We shall now describe these modes one by one.

3.2. Geostrophic balance

For the continuous equations before discretisation, geostrophically balanced modes are obtained from non-zero steady solutions of the equations. As shown in Cotter et al. [4], in the $P1_{DG}$–$P2$ discretisation solutions which satisfy the geostrophic balance relation are also exactly steady. To see this within the framework of this paper, assume a steady state, then Eqs. (4)–(8) become

$$-f\langle\nabla\alpha^\delta,\nabla\psi^\delta\rangle + c^2\langle\nabla\alpha^\delta,\nabla\eta^\delta\rangle = 0, \tag{9}$$

$$f\langle\nabla\alpha^\delta,\nabla\phi^\delta\rangle = 0, \tag{10}$$

$$-\langle\nabla\alpha^\delta,\nabla\phi^\delta\rangle = 0, \tag{11}$$

$$f\langle\bar{\boldsymbol{w}}^\delta,\bar{\boldsymbol{u}}^\delta\rangle = 0, \tag{12}$$

$$f\langle\hat{\boldsymbol{w}}^\delta,(\hat{\boldsymbol{u}}^\delta)^\perp\rangle = 0. \tag{13}$$

Eqs. (10) and (11) both imply that $\phi^\delta = 0$ since they are the usual continuous finite element discretisations of the Laplace equation which has no non-zero solutions because ϕ^δ and α^δ are both restricted to $\overline{P2}$. Similarly Eqs. (12) and (13) imply that $\bar{\boldsymbol{u}}^\delta = \hat{\boldsymbol{u}}^\delta = \boldsymbol{0}$. Eq. (9) is the discrete geostrophic balance relation between ψ^δ and η^δ, and the Laplace operator can be inverted (since the finite element discretisation of the Poisson equation has a unique solution for solutions in $\overline{P2}$) to obtain the *pointwise* geostrophic balance relation

$$f\psi^\delta = c^2\eta^\delta,$$

as noted in Cotter et al. [4]. This means that $P1_{DG}$–$P2$ has an excellent representation of geostrophic balance.

3.3. Inertia gravity waves

The physical wave variables ϕ^δ, ψ^δ and η^δ are uncoupled from the mean velocity component $\bar{\boldsymbol{u}}^\delta$ and the spurious velocity component $\hat{\boldsymbol{u}}^\delta$. To obtain the discrete inertia gravity wave equation, the time derivative applied to Eq. (4) gives

$$\frac{\mathrm{d}^2}{\mathrm{d}t^2}\langle\nabla\alpha^\delta,\nabla\phi^\delta\rangle - f\frac{\mathrm{d}}{\mathrm{d}t}\langle\nabla\alpha^\delta,\nabla\psi^\delta\rangle + \frac{\mathrm{d}}{\mathrm{d}t}c^2\langle\nabla\alpha^\delta,\nabla\eta^\delta\rangle = 0.$$

Substitution of Eqs. (5) and (6) then give

$$\left(\frac{\mathrm{d}^2}{\mathrm{d}t^2}+f^2\right)\frac{\mathrm{d}}{\mathrm{d}t}\langle\alpha^\delta,\eta^\delta\rangle + \frac{\mathrm{d}}{\mathrm{d}t}c^2\langle\nabla\alpha^\delta,\nabla\eta^\delta\rangle = 0. \tag{14}$$

This is the usual continuous finite element discretisation of the inertia–gravity wave equation

$$\left(\frac{\partial^2}{\partial t^2}+f^2\right)\frac{\partial}{\partial t}\eta - c^2\nabla^2\frac{\partial\eta}{\partial t} = 0. \tag{15}$$

Since only $P2$ functions are present, the solution η^δ is third-order accurate, as opposed to the second-order accuracy expected with a first-order velocity discretisation. This higher-than-expected accuracy means that $P1_{DG}$–$P2$ has a very accurate representation of inertia–gravity wave propagation. In particular, it should be expected that the phase velocity is more independent of mesh orientation than other second-order methods. The equivalent property for $P0$–$P1$ was noted in Roux et al. [16], namely that the inertia–gravity dispersion relation was one order more accurate than expected, namely second-order. The above proof extends this result to both arbitrary meshes, and to any finite element pair that satisfies the embedding properties above.

A numerical verification of this third-order convergence is shown in Fig. 1. Care must be taken to obtain third-order convergence: if the initial conditions for the $P1_{DG}$ velocity are obtained by $P1_{DG}$ collocation, i.e. evaluating the analytic initial condition at the node points and using those values as nodal basis coefficients, then the truncation error in the initial condition for the velocity is second-order, and hence second-order accuracy is the most that can be expected after time-integrating the equations. However, a third-order accurate velocity initial condition can be obtained by first constructing a higher-order finite element approximation to the velocity field by collocation (we used a $P2$ approximation in the calculations in Fig. 1), and then applying the L_2 projection to obtain a $P1_{DG}$ velocity field. This results in third-order convergence of the free surface elevation over fixed time, since the free surface elevation equation is the $P2$ finite element approximation to the inertia–gravity wave equation, as shown above. To see that this procedure leads to a third-order accurate velocity field initial condition, first write the analytic initial condition for the velocity as

$$\boldsymbol{u}(\boldsymbol{x},0) = \nabla\phi_0 + \nabla^\perp\psi_0 + \bar{\boldsymbol{u}}_0.$$

By standard approximation theory, the pth-order collocated finite element approximation to the initial condition satisfies $\boldsymbol{u}^p = \boldsymbol{u}(\boldsymbol{x},0) + \mathcal{O}(\Delta x^{p+1})$. The $P1_{DG}$–$P2$ initial condition $\boldsymbol{u}^\delta$ satisfies

$$\int \boldsymbol{v}^\delta \cdot \boldsymbol{u}^\delta \mathrm{d}V = \int \boldsymbol{v}^\delta \cdot \boldsymbol{u}^p \mathrm{d}V$$

for all $P1_{DG}$ test functions $\boldsymbol{v}^\delta$. After subsitution of the Helmholtz decomposition for $\boldsymbol{u}(\boldsymbol{x},0)$ and the discrete Helmholtz decomposition for $\boldsymbol{u}^\delta$, this becomes

$$\int \nabla\alpha^\delta \cdot \nabla\phi^\delta \mathrm{d}V = \int \nabla\alpha^\delta \cdot \nabla\phi_0 \mathrm{d}V + \mathcal{O}(\Delta x^{p+1}),$$
$$\int \nabla\alpha^\delta \cdot \nabla\psi^\delta \mathrm{d}V = \int \nabla\alpha^\delta \cdot \nabla\psi_0 \mathrm{d}V + \mathcal{O}(\Delta x^{p+1}),$$
$$\bar{\boldsymbol{u}}^\delta = \bar{\boldsymbol{u}}_0 + \mathcal{O}(\Delta x^{p+1})$$

and the potentials ϕ^δ and ψ^δ converge to ϕ_0 and ψ_0 as $\mathcal{O}(\Delta x^3)$ following standard convergence theory for finite element discretisations of elliptic problems (see [2], for example). Third-order convergence for the $P1_{DG}$–$P2$ discretisation applied to inertia–gravity waves on the f-plane was demonstrated in Comblen et al. [3] in which various partly-discontinuous finite element pairs were benchmarked against a high-order discontinuous Galerkin reference solution. Since the initial conditions were obtained by L_2 projection from the high-order solution, third-order convergence was observed.

3.4. Physical inertial oscillation

Since the integration is performed over spatially-independent functions, Eq. (7) may be written as

$$\bar{\boldsymbol{w}}^\delta \cdot \left(\frac{\mathrm{d}}{\mathrm{d}t}\bar{\boldsymbol{u}}^\delta + f(\bar{\boldsymbol{u}}^\delta)^\perp \right) = 0$$

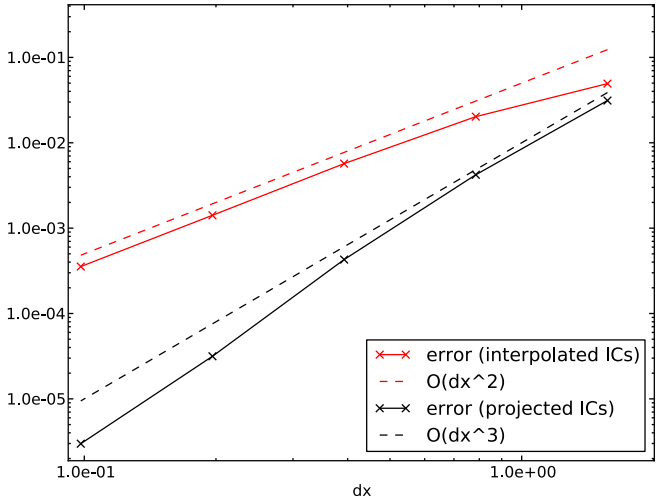

Fig. 1. Plot showing convergence rates for the $P1_{DG}$–$P2$ discretisation applied to the linear rotating shallow-water equations on an f-plane. The test problem is a single propagating sinusoidal wave in periodic boundary conditions, with the L_2 error in the free surface elevation computed after the wave has propagated all the way around the periodic domain. Second-order convergence for the free surface elevation is obtained when the initial conditions for velocity are obtained by collocation at node points; third-order convergence for the free surface elevation is obtained when the initial conditions are obtained by collocation with a quadratic $P2$ basis for velocity and reduced to the $P1_{DG}$ space by L_2 projection.

and since it must hold for all $\bar{\boldsymbol{w}}^\delta$, we obtain

$$\frac{\mathrm{d}}{\mathrm{d}t}\bar{\boldsymbol{u}}^\delta + f(\bar{\boldsymbol{u}}^\delta)^\perp = 0,$$

which is the usual inertial oscillation equation which has spatially-independent solutions which rotate with frequency f.

3.5. Spurious inertial oscillations

Eq. (8) describes the dynamics of the spurious velocity component $\hat{\boldsymbol{u}}^\delta$. If $\hat{\boldsymbol{u}}^\delta$ is a spurious velocity (i.e. is orthogonal to all $\nabla\alpha^\delta$ and $\nabla^\perp\alpha^\delta$), then so is $(\hat{\boldsymbol{u}}^\delta)^\perp$ and so Eq. (8) does not involve any projection and hence can be written as

$$\frac{\mathrm{d}}{\mathrm{d}t}\hat{\boldsymbol{u}}^\delta + f(\hat{\boldsymbol{u}}^\delta)^\perp = 0$$

these solutions also simply rotate with frequency f and hence must be interpreted as spurious inertial oscillations which do not propagate as waves.

If we replace the velocity space $P1_{DG}$ with the restricted space $H(P2)$, as described in Section 2, then we obtain the finite element pair which we call $H(P2)$–$P2$. we still have Eqs. (4)–(7) but without the spurious inertial oscillations in Eq. (8), hence the $H(P2)$–$P2$ discretisation has no spurious modes.

3.6. Discrete dispersion relation for inertia-gravity waves

In this section, we compute the discrete dispersion relation for the $P1_{DG}$–$P2$ discretisation applied to the rotating shallow-water equations on the f-plane for the special case of a structured mesh in a regular hexagonal domain with edge length L centred on the origin, with periodic boundary conditions for opposing faces, tiled with equilateral triangles with edge lengths $\Delta x = L/N$ for some positive integer N, and use this to define a continuous $P2$ finite element mesh. The discrete dispersion relation is developed by searching for time-harmonic solutions of (14). Assuming such a time-harmonic solution $\eta^\delta \propto e^{i\omega t}$, Eq. (14) becomes

$$(-\omega^2 + f^2)\langle\alpha^\delta, \eta^\delta\rangle + c^2\langle\nabla\alpha^\delta, \nabla\eta^\delta\rangle = 0. \tag{16}$$

If η^δ is an eigensolution of Eq. (16), then so is $T_{\boldsymbol{z}}\eta^\delta(\boldsymbol{x}) = \eta^\delta(\boldsymbol{x} - \boldsymbol{z})$ for any $\boldsymbol{z}$ in the set $\mathbb{V}$ of translations that map vertices in the mesh to other vertices. Hence, eigenfunctions of Eq. (16) are all eigenfunctions of $T_{\boldsymbol{z}}$, i.e. they take the form

$$\eta^\delta(\boldsymbol{x})|_{\boldsymbol{x}\in\Omega_{\boldsymbol{z}}} = \hat{\eta}^\delta(\xi)e^{i\boldsymbol{k}\cdot\boldsymbol{z}}, \quad \xi\Delta x + \boldsymbol{z} = \boldsymbol{x}, \quad \forall \boldsymbol{z} \in \mathbb{V}, \tag{17}$$

where $\Omega_{\boldsymbol{z}}$ is the translation of the hexagon formed from the six equilateral triangles surrounding the vertex at the origin by $\boldsymbol{z}$, $\hat{\eta}^\delta(\xi)$ is defined on the reference hexagon Ω_e with edge length 1 and centred at the origin, ξ is the local coordinate in Ω_e, and $\boldsymbol{k} \in \mathbb{R}^2$ is the wave vector satisfying $\boldsymbol{k}\cdot\boldsymbol{z} = 2\pi l$ with l an integer. The wave vector $\boldsymbol{k}$ is contained in the first Brillouin zone of the periodic hexagonal domain which is bounded by the lines

$$\boldsymbol{k}\cdot(\cos(\theta_n), \sin(\theta_n))^T = \frac{2}{\sqrt{3}}\pi, \quad \theta_n = \left(n + \frac{1}{2}\right)\pi/3, \quad \text{for } n = 1, 2, \ldots, 6.$$

For more details of functions on periodic lattices, see [8], for example.

Let us now fix an arbitrary wave vector $\boldsymbol{k}$ satisfying the conditions above. We note that the integral in Eq. (16) can be performed by integrating over all hexagons $\Omega_{\boldsymbol{z}}$ and dividing by three (since each equilateral triangle is covered by three hexagons). Given a test function α^δ, Eq. (16) (multiplied by three) becomes

$$\begin{aligned}
0 &= \sum_{\boldsymbol{z}\in\mathbb{V}} \int_{\Omega_{\boldsymbol{z}}} (-\omega^2 + f^2)\alpha^\delta(\boldsymbol{x})\eta^\delta(\boldsymbol{x}) + c^2\nabla\alpha^\delta(\boldsymbol{x})\cdot\nabla\eta^\delta(\boldsymbol{x})\mathrm{d}V(\boldsymbol{x}) \\
&= \sum_{\boldsymbol{z}\in\mathbb{V}} \int_{\Omega_e} (\Delta x^2(-\omega^2 + f^2)\alpha^\delta(\xi\Delta x + \boldsymbol{z})\hat{\eta}^\delta(\xi) + \nabla_\xi\alpha^\delta(\xi\Delta x + \boldsymbol{z})\cdot\nabla_\xi\hat{\eta}^\delta(\xi))e^{i\boldsymbol{k}\cdot\boldsymbol{z}}\mathrm{d}V(\xi) \\
&= \int_{\Omega_e} \Delta x^2(-\omega^2 + f^2)\hat{\alpha}^\delta(\xi)\hat{\eta}^\delta(\xi) + c^2\nabla\hat{\alpha}^\delta(\xi)\cdot\nabla\hat{\eta}^\delta(\xi)\mathrm{d}V(\xi),
\end{aligned}$$

where $\hat{\alpha}^\delta$ is defined on Ω_e with

$$\hat{\alpha}^\delta(\xi) = \sum_{\boldsymbol{z}\in\mathbb{V}} \alpha^\delta(\xi\Delta x - \boldsymbol{z})e^{i\boldsymbol{k}\cdot\boldsymbol{z}}.$$

We have now written the dispersion relation in such a way that all the computations can be done over one single reference hexagon Ω_e. The boundary conditions for $\hat{\eta}^\delta$ on the reference hexagon can be computed from the condition that $\hat{\eta}^\delta$ is continuous at the boundaries, meaning that on each edge of the hexagon Ω_e, denoted $\partial\Omega_{e,n}$ (with $1 \leqslant n \leqslant 6$),

$$\hat{\eta}^\delta(\xi) = e^{i\Delta x\boldsymbol{k}\cdot\Delta\xi}\hat{\eta}^\delta(\xi + \Delta\xi),$$

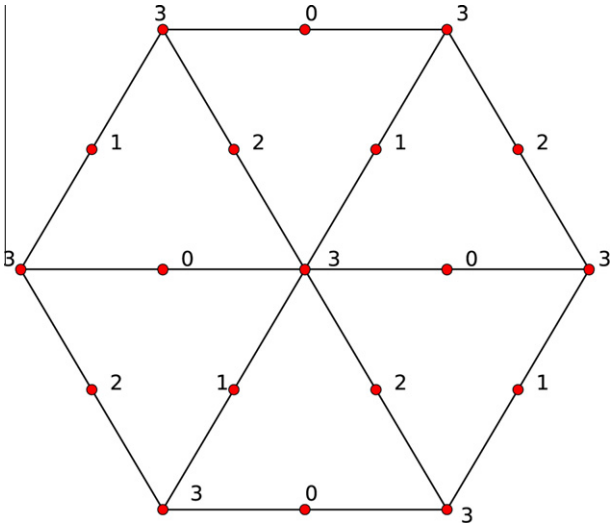

Fig. 2. Diagram showing the reference domain Ω_e which is used to perform the numerical dispersion relation calculations. After considering the boundary conditions for $\hat{\eta}^\delta$ which are the consequence of requiring that η^δ is continuous, there are four degrees of freedom for $\hat{\eta}^\delta$, which we denote $\{\tilde{\eta}_n\}_{n=0}^4$. Each node in the diagram is labelled with a number n, indicating that $\hat{\eta}^\delta = \tilde{\eta}_n e^{i\boldsymbol{k}\cdot\boldsymbol{\xi}\Delta x}$ at that node.

where $\Delta\boldsymbol{\xi}$ is the vector from $\partial\Omega_{e,n}$ to the opposing face. Fig. 2 illustrates the consequences of this for the basis coefficients of $\hat{\eta}^\delta$ when a nodal basis[1] is used.

We can similarly use continuity of α^δ to obtain boundary conditions for $\hat{\alpha}^\delta(\boldsymbol{\xi})$ on $\partial\Omega_e$. On the boundary $\partial\Omega_{e,n}$,

$$\begin{aligned}\hat{\alpha}^\delta(\boldsymbol{\xi}) &= \sum_{\boldsymbol{z}\in\mathbb{V}} \alpha^\delta(\boldsymbol{\xi}\Delta x - \boldsymbol{z}) e^{i\boldsymbol{k}\cdot\boldsymbol{z}},\\ &= \sum_{\boldsymbol{z}\in\mathbb{V}} \alpha^\delta((\boldsymbol{\xi}+\Delta\boldsymbol{\xi})\Delta x - (\boldsymbol{z}+\Delta x\Delta\boldsymbol{\xi})) e^{i\boldsymbol{k}\cdot\boldsymbol{z}},\\ &= \sum_{\boldsymbol{z}\in\mathbb{V}} \alpha^\delta((\boldsymbol{\xi}-\Delta\boldsymbol{\xi})\Delta x - \boldsymbol{z}) e^{i\boldsymbol{k}\cdot(\boldsymbol{z}-\Delta x\Delta\boldsymbol{\xi})},\\ &= e^{-i\Delta x\boldsymbol{k}\cdot\boldsymbol{\xi}}\hat{\alpha}^\delta(e^{\Delta\boldsymbol{\xi}}+\Delta\boldsymbol{\xi}).\end{aligned}$$

This means that $\hat{\alpha}^\delta$ has boundary conditions which are the complex conjugate of the boundary conditions for $\hat{\eta}^\delta$.

We adopt a nodal basis for functions inside Ω_e. There are 19 $P2$ nodes on Ω_e (see Fig. 2), and so we write

$$\hat{\eta}^\delta = \sum_{n=1}^{19} \hat{\eta}_n N_n(\boldsymbol{\xi}),$$

where $N_n(\boldsymbol{\xi})$, $(n = 1,\ldots,19)$, are the nodal basis functions for $P2$ functions inside Ω_e, and η_n $(n = 1,\ldots,19)$ are the nodal basis coefficients. The boundary conditions for $\hat{\eta}^\delta$ described above can be expressed *via* a matrix S (which is a function of $\boldsymbol{k}\Delta x$ due to the dependence of the boundary conditions for $\hat{\eta}$ and $\hat{\alpha}$ on $\boldsymbol{k}$), so that

$$\hat{\boldsymbol{\eta}} = S\tilde{\boldsymbol{\eta}}, \quad \hat{\boldsymbol{\alpha}} = S^*\tilde{\boldsymbol{\alpha}},$$

where $\hat{\boldsymbol{\eta}}$ and $\hat{\boldsymbol{\alpha}}$ are the vectors of the basis coefficients of η^δ and α^δ, respectively, and $\tilde{\boldsymbol{\eta}}$ and $\tilde{\boldsymbol{\alpha}}$ are the corresponding vectors of the independent degrees of freedom.

After substituting, the wave equation becomes

$$0 = (-\omega^2+f^2)\langle\alpha^\delta,\eta^\delta\rangle + g\langle\nabla\alpha^\delta,\nabla\eta^\delta\rangle = 0 = \Delta x^2\hat{\boldsymbol{\alpha}}^T\left((-\omega^2+f^2)M_e + \frac{gL_e}{\Delta x^2}\right)\hat{\boldsymbol{\eta}} = \Delta x^2\tilde{\boldsymbol{\alpha}}^T S^\dagger\left((-\omega^2+f^2)M_e + g\frac{L_e}{\Delta x^2}\right)S\tilde{\boldsymbol{\eta}},$$

where M_e is the local mass matrix

$$M_{e,ij} = \int_{\Omega_e} N_i(\boldsymbol{\xi})N_j(\boldsymbol{\xi})\mathrm{d}V(\boldsymbol{\xi})$$

and L_e is the Laplacian matrix

[1] A nodal basis is a basis in which each basis function has unit value at one of the node points, e.g. the vertices and edge midpoints in the case of the continuous quadratic mesh, and vanishes on all other node points.

$$L_{e,ij} = \int_{\Omega_e} \nabla N_i(\boldsymbol{\xi}) \cdot \nabla N_j(\boldsymbol{\xi}) \mathrm{d}V(\boldsymbol{\xi})$$

and † indicates the Hermitian conjugate of a matrix. Since $\tilde{\boldsymbol{\alpha}}$ is arbitrary, we seek non-trivial solutions of

$$S^\dagger(\Delta x^2(-\omega^2 + f^2)M_e + gL_e)S\tilde{\boldsymbol{\eta}} = \mathbf{0}$$

and we obtain the dispersion relation

$$|S^\dagger(\Delta x^2(-\omega^2 + f^2)M_e + gL_e)S| = 0, \tag{18}$$

which must be solved for ω given $\boldsymbol{k}$ (the $\boldsymbol{k}$ dependence is in S as described above). This equation is the determinant of a 4×4 matrix with entries that are linear in $\lambda = \Delta x^2(\omega^2 - f^2)$, so it is a quartic polynomial in λ.

After lengthy calculation using SymPy [18], the following matrices are obtained:

$$S^\dagger M_e S = \begin{pmatrix} A & B \\ B^T & C \end{pmatrix}, \quad S^\dagger L_e S = \begin{pmatrix} D & E \\ E^T & F \end{pmatrix},$$

where

$$A = \begin{pmatrix} \frac{4}{15}\sqrt{3} & \frac{2}{15}\sqrt{3}\cos\left(-\frac{1}{4}k + \frac{1}{4}l\sqrt{3}\right) \\ \frac{2}{15}\sqrt{3}\cos\left(-\frac{1}{4}k + \frac{1}{4}l\sqrt{3}\right) & \frac{4}{15}\sqrt{3} \end{pmatrix},$$

$$B = \begin{pmatrix} \frac{2}{15}\sqrt{3}\cos\left(\frac{1}{4}k + \frac{1}{4}l\sqrt{3}\right) & \frac{2}{15}\sqrt{3}\cos\left(\frac{1}{2}k\right) \\ -\frac{1}{30}\sqrt{3}\cos\left(\frac{1}{2}l\sqrt{3}\right) & -\frac{1}{30}\sqrt{3}\cos\left(\frac{3}{4}k - \frac{1}{4}l\sqrt{3}\right) \end{pmatrix},$$

$$C = \begin{pmatrix} \frac{4}{15}\sqrt{3} & -\frac{1}{30}\sqrt{3}\cos\left(\frac{3}{4}k + \frac{1}{4}l\sqrt{3}\right) \\ -\frac{1}{30}\sqrt{3}\cos\left(\frac{3}{4}k + \frac{1}{4}l\sqrt{3}\right) & -\frac{1}{60}\sqrt{3}\cos(k) - \frac{1}{60}\sqrt{3}\cos\left(\frac{1}{2}k + \frac{1}{2}l\sqrt{3}\right) - \frac{1}{60}\sqrt{3}\cos\left(-\frac{1}{2}k + \frac{1}{2}l\sqrt{3}\right) + \frac{3}{20}\sqrt{3} \end{pmatrix},$$

$$D = \begin{pmatrix} 8\sqrt{3} & -\frac{8}{3}\sqrt{3}\cos\left(-\frac{1}{4}k + \frac{1}{4}l\sqrt{3}\right) \\ -\frac{8}{3}\sqrt{3}\cos\left(-\frac{1}{4}k + \frac{1}{4}l\sqrt{3}\right) & 8\sqrt{3} \end{pmatrix},$$

$$E = \begin{pmatrix} -\frac{8}{3}\sqrt{3}\cos\left(\frac{1}{4}k + \frac{1}{4}l\sqrt{3}\right) & -\frac{8}{3}\sqrt{3}\cos\left(\frac{1}{2}k\right) \\ -\frac{8}{3}\sqrt{3}\cos\left(\frac{1}{2}k\right) & -\frac{8}{3}\sqrt{3}\cos\left(\frac{1}{4}k + \frac{1}{4}l\sqrt{3}\right) \end{pmatrix} \quad \text{and}$$

$$F = \begin{pmatrix} 8\sqrt{3} & -\frac{8}{3}\sqrt{3}\cos\left(-\frac{1}{4}k + \frac{1}{4}l\sqrt{3}\right) \\ -\frac{8}{3}\sqrt{3}\cos\left(-\frac{1}{4}k + \frac{1}{4}l\sqrt{3}\right) & \frac{2}{3}\sqrt{3}\cos\left(-\frac{1}{2}k + \frac{1}{2}l\sqrt{3}\right) + \frac{2}{3}\sqrt{3}\cos(k) + \frac{2}{3}\sqrt{3}\cos\left(\frac{1}{2}k + \frac{1}{2}l\sqrt{3}\right) + 6\sqrt{3} \end{pmatrix},$$

having written $\boldsymbol{k} = (k, l)$.

The resulting quartic equation for $\lambda = \Delta x^2(\omega^2 - f^2)$ obtained from evaluating the determinant (18) is a very complicated expression that would take up several pages. Hence, solutions to the dispersion relation Eq. (18) were obtained by numerically evaluating the matrix $(S^\dagger M_e S)^{-1} S^\dagger L_e S$ for various values of $\boldsymbol{k}$, and using the Scientific Python `linalg.eig` routine, which were then sorted in numerical order. Since the equation for $\lambda = \Delta x^2(\omega^2 - f^2)$ is quartic, this leads to four branches of the dispersion relation (this is typical for $P2$ schemes in two dimensions), which correspond to the fundamental $\exp(i\boldsymbol{k} \cdot \boldsymbol{x})$ modes with $\boldsymbol{k}$ inside the first Brillouin zone, plus higher wave number solutions obtained from the second, third and fourth Brillouin zones which have the same translation property at the triangle vertices but result in different values at the edge centres. The plots of the four branches are given in Fig. 3. It is immediately visible that the lowest eigenvalues are very isotropic, as might be expected from the fact that the dispersion relation is in fact third-order rather than second-order, as described in Section 3.3. This means that resolved gravity waves of a particular wave number have a propagation speed which is largely independent of the direction of alignment of the mesh (this is a property which is considered important and was one of the contributing factors towards designing the hexagonal C-grid as an alternative to the triangular C-grid). It can also be seen that the dispersion relation is monotonically-increasing with $|\boldsymbol{k}|$ with some small jumps when moving between branches (see Cotter et al. [5] for the equivalent one-dimensional plot); there are no spurious inertia–gravity modes.

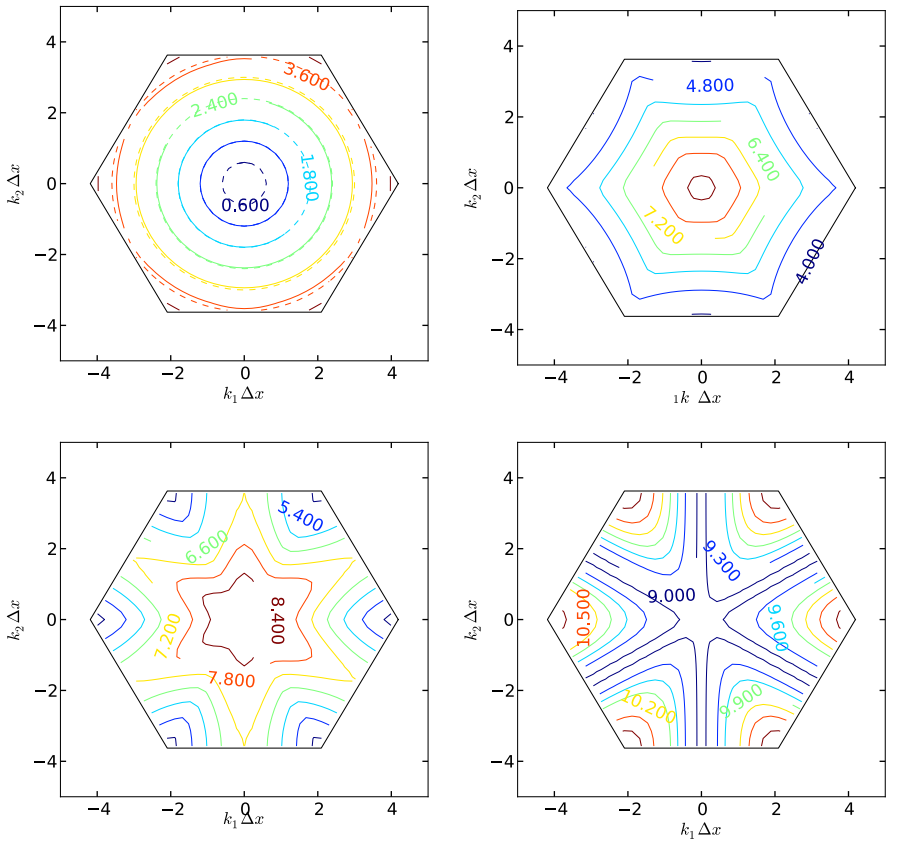

Fig. 3. Plots showing contours of $\Delta x(\omega^2 - f^2)$ in the $\boldsymbol{k}\Delta x$ plane for each of the four branches of the numerical dispersion relation for the $P1_{DG}$–$P2$ finite element scheme applied to the linear rotating shallow water equations on the f-plane. The lowest branch is shown top-left, with contours of the exact dispersion relation superimposed using dashed lines. This lowest branch is very accurate, and the contours are very circular, meaning that the wave propagation is almost independent of the direction of mesh alignment. The other plots show the higher branches which represent the second, third and fourth Brillouin zones in the $\boldsymbol{k}\Delta x$ plane mapped in to the first Brillouin zone. For example, one can cross from the lowest branch into the branch in the top-right branch by going through the hexagon which bounds the region, emerging from the opposite edge in the hexagon in the top-right plot, moving in the opposite direction. It can be seen that all four branches represent physical modes from different regions of physical $\boldsymbol{k}$-space which can be resolved on the grid.

4. Discrete wave propagation on the β-plane

In this section, we consider the quasi-geostrophic scaling on the β-plane, following the approach of Roux and Pouliot [15], and Thuburn [19], in which the quasi-geostrophic approximation is applied to the spatially-discretised equations.

In the β-plane case, $f = f_0 + \beta y$, and after substitution of the orthogonal decomposition for the solution variables and test functions into Eqs. (2) and (3) we obtain

$$\frac{\mathrm{d}}{\mathrm{d}t}\langle\nabla\alpha^\delta,\nabla\phi^\delta\rangle - f_0\langle\nabla\alpha^\delta,\nabla\psi^\delta\rangle - \langle\beta y\nabla\alpha^\delta,\bar{\boldsymbol{u}}^\delta + (\hat{\boldsymbol{u}}^\delta)^\perp + \nabla\psi^\delta + \nabla^\perp\phi^\delta\rangle + c^2\langle\nabla\alpha^\delta,\nabla\eta^\delta\rangle = 0,$$

$$\frac{\mathrm{d}}{\mathrm{d}t}\langle\nabla\alpha^\delta,\nabla\psi^\delta\rangle + f_0\langle\nabla\alpha^\delta,\nabla\phi^\delta\rangle + \langle\beta y\nabla\alpha^\delta,-\bar{\boldsymbol{u}}^\delta - \hat{\boldsymbol{u}}^\delta + \nabla^\perp\phi^\delta + \nabla\psi^\delta\rangle = 0,$$

$$\frac{\mathrm{d}}{\mathrm{d}t}\langle\alpha^\delta,\eta^\delta\rangle - \langle\nabla\alpha^\delta,\nabla\phi^\delta\rangle = 0,$$

$$\frac{\mathrm{d}}{\mathrm{d}t}\langle\bar{\boldsymbol{w}}^\delta,\bar{\boldsymbol{u}}^\delta\rangle + f_0\langle\bar{\boldsymbol{w}}^\delta,(\bar{\boldsymbol{u}}^\delta)^\perp\rangle + \langle\bar{\boldsymbol{w}}^\delta\beta y,(\bar{\boldsymbol{u}}^\delta)^\perp + (\hat{\boldsymbol{u}}^\delta)^\perp + \nabla^\perp\phi^\delta - \nabla\psi^\delta\rangle = 0,$$

$$\frac{\mathrm{d}}{\mathrm{d}t}\langle\hat{\boldsymbol{w}}^\delta,\hat{\boldsymbol{u}}^\delta\rangle + f_0\langle\hat{\boldsymbol{w}}^\delta,(\hat{\boldsymbol{u}}^\delta)^\perp\rangle + \langle\hat{\boldsymbol{w}}^\delta\beta y,(\bar{\boldsymbol{u}}^\delta)^\perp + (\hat{\boldsymbol{u}}^\delta)^\perp + \nabla^\perp\phi^\delta - \nabla\psi^\delta\rangle = 0.$$

At leading order in Rossby number in the quasi-geostrophic scaling, we obtain the geostrophic balance:

$$
\begin{aligned}
&-f_0\left\langle \nabla\alpha^\delta, \nabla\psi_g^\delta\right\rangle + c^2\left\langle \nabla\alpha^\delta, \nabla\eta_g^\delta\right\rangle = 0,\\
&f_0\left\langle \nabla\alpha^\delta, \nabla\phi_g^\delta\right\rangle = 0,\\
&-\left\langle \nabla\alpha^\delta, \nabla\phi_g^\delta\right\rangle = 0,\\
&f_0\left\langle \hat{\boldsymbol{w}}^\delta, (\hat{\boldsymbol{u}}^\delta)_g^\perp\right\rangle = 0,
\end{aligned}
$$

which we have already analysed in Section 3.2, and so we know that it implies that

$$\hat{\boldsymbol{u}}_g^\delta = 0, \quad \phi_g^\delta = 0, \quad \psi_g^\delta = \frac{c^2}{f}\eta_g^\delta. \tag{19}$$

At the next order we obtain

$$\frac{\mathrm{d}}{\mathrm{d}t}\left\langle \nabla\alpha^\delta, \nabla\phi_{ag}^\delta\right\rangle - f_0\left\langle \nabla\alpha^\delta, \nabla\psi_{ag}^\delta\right\rangle - \left\langle \beta y\nabla\alpha^\delta, \nabla\psi_g^\delta\right\rangle + gH\left\langle \nabla\alpha^\delta, \nabla\eta_{ag}^\delta\right\rangle = 0, \tag{20}$$

$$\frac{\mathrm{d}}{\mathrm{d}t}\left\langle \nabla\alpha^\delta, \nabla\psi_g^\delta\right\rangle + f_0\left\langle \nabla\alpha^\delta, \nabla\phi_{ag}^\delta\right\rangle + \left\langle \beta y\nabla\alpha^\delta, \nabla^\perp\psi_g^\delta\right\rangle = 0, \tag{21}$$

$$\frac{\mathrm{d}}{\mathrm{d}t}\left\langle \alpha^\delta, \eta_g^\delta\right\rangle - \left\langle \nabla\alpha^\delta, \nabla\phi_{ag}^\delta\right\rangle = 0, \tag{22}$$

$$f_0\left\langle \bar{\boldsymbol{w}}^\delta, (\bar{\boldsymbol{u}}^\delta)_{ag}^\perp\right\rangle + \left\langle \bar{\boldsymbol{w}}^\delta\beta y, -\nabla\psi_g^\delta\right\rangle = 0, \tag{23}$$

$$f_0\left\langle \hat{\boldsymbol{w}}^\delta, (\hat{\boldsymbol{u}}^\delta)_{ag}^\perp\right\rangle + \left\langle \hat{\boldsymbol{w}}^\delta\beta y, -\nabla\psi_g^\delta\right\rangle = 0. \tag{24}$$

Notice that the spurious velocity modes do not appear at this order in the physical mode Eqs. (20)–(22), and that Eq. (24) states that the ageostrophic spurious velocity modes are slaved to the geostrophic streamfunction. Substituting Eqs. (19) and (22) into (21) gives

$$\frac{\mathrm{d}}{\mathrm{d}t}\left(\left\langle \nabla\alpha^\delta, \nabla\psi_g^\delta\right\rangle + \frac{f_0^2}{gH}\left\langle \alpha^\delta, \psi_g^\delta\right\rangle\right) + \left\langle \beta y\nabla\alpha^\delta, \nabla^\perp\psi_g^\delta\right\rangle = 0. \tag{25}$$

The second term in Eq. (25) may be written as

$$\left\langle \beta y\nabla\alpha^\delta, \nabla^\perp\psi_g^\delta\right\rangle = \left\langle \nabla(\beta y\alpha^\delta) - \beta\alpha^\delta(0,1), \nabla^\perp\psi_g^\delta\right\rangle = -\beta\left\langle \alpha^\delta, \frac{\partial}{\partial x}\psi_g^\delta\right\rangle$$

and we obtain the usual continuous finite element approximation to the Rossby wave equation using $P2$ elements

$$\frac{\mathrm{d}}{\mathrm{d}t}\left(\left\langle \nabla\alpha^\delta, \nabla\psi_g^\delta\right\rangle + \frac{f_0^2}{gH}\left\langle \alpha^\delta, \psi_g^\delta\right\rangle\right) - \beta\left\langle \alpha^\delta, \frac{\partial}{\partial x}\psi_g^\delta\right\rangle = 0. \tag{26}$$

Since $P2$ elements are used, the approximation to the Rossby wave equation is third-order accurate, rather than the second-order accuracy one would expect with $P1_{DG}$ for velocity. The equivalent property for $P0$–$P1$ was shown in Roux and Pouliot [15], namely that the Rossby wave dispersion relation is second-order. The above proof extends this result to arbitrary meshes and to any finite element pair which satisfies the embedding properties.

We again expect that the phase velocity is more independent of mesh orientation than other second-order methods. Since the streamfunction ψ^δ and the height variable η^δ are both from the $P2$ space and hence have the same numbers of degrees of freedom, there are exactly twice as many inertia–gravity wave modes as Rossby wave modes. We also note that if the reduced space $H(P2)$–$P2$ is used instead of $P1_{DG}$–$P2$ we obtain the same equations but with vanishing spurious inertial modes.

4.1. Discrete dispersion relation for Rossby waves

Starting from Eq. (26), and following the method described above for the obtaining the inertia-gravity wave dispersion relation on the equilateral grid, we obtain the numerical dispersion relation

$$\left|S^\dagger\left(i\omega\left(\frac{L_e}{\Delta x^2} + \frac{1}{L_R^2}M_e\right) - \beta\frac{D_e}{\Delta x}\right)S\right| = 0, \tag{27}$$

where D_e is the local derivative matrix

$$D_{e,ij} = \int_{\Omega_e} N_i(\xi)\hat{\boldsymbol{f}}\cdot\nabla N_j(\xi)\mathrm{d}V(\xi)$$

and where $\hat{\boldsymbol{f}}$ is the unit vector pointing in the direction of increasing f on the β-plane. We shall investigate the variation in the dispersion relation with the alignment of the triangular grid, and hence it is convenient to write

$$D_{e,ij} = \hat{f}_1 D^1_{e,ij} + \hat{f}_2 D^2_{e,ij},$$

where

$$D^1_{e,ij} = \int_{\Omega_e} N_i(\xi) \frac{\partial N_j}{\partial \xi_1}(\xi) \mathrm{d}V(\xi), \quad D^2_{e,ij} = \int_{\Omega_e} N_i(\xi) \frac{\partial N_j}{\partial \xi_2}(\xi) \mathrm{d}V(\xi).$$

After further algebraic manipulation with SymPy, we obtain

$$S^\dagger D^1_e S = \begin{pmatrix} P_1 & Q_1 \\ Q_1^T & R_1 \end{pmatrix}, \quad S^\dagger L_e S = \begin{pmatrix} P_2 & Q_2 \\ Q_2^T & R_2 \end{pmatrix},$$

where

$$P_1 = \begin{pmatrix} 0 & -\frac{2}{5}\sqrt{3}\sin\left(-\frac{1}{4}k + \frac{1}{4}l\sqrt{3}\right) \\ -\frac{2}{5}\sqrt{3}\sin\left(-\frac{1}{4}k + \frac{1}{4}l\sqrt{3}\right) & 0 \end{pmatrix},$$

$$Q_1 = \begin{pmatrix} \frac{2}{5}\sqrt{3}\sin\left(\frac{1}{4}k + \frac{1}{4}l\sqrt{3}\right) & \frac{4}{5}\sqrt{3}\sin\left(\frac{1}{2}k\right) \\ \frac{3}{5}\sqrt{3}\sin\left(\frac{1}{2}k\right) & -\frac{1}{10}\sqrt{3}\sin\left(\frac{3}{4}k - \frac{1}{4}l\sqrt{3}\right) + \frac{3}{10}\sqrt{3}\sin\left(\frac{1}{4}k + \frac{1}{4}l\sqrt{3}\right) \end{pmatrix},$$

$$R_1 = \begin{pmatrix} 0 & -\frac{3}{10}\sqrt{3}\sin\left(-\frac{1}{4}k + \frac{1}{4}l\sqrt{3}\right) - \frac{1}{10}\sqrt{3}\sin\left(\frac{3}{4}k + \frac{1}{4}l\sqrt{3}\right) \\ -\frac{3}{10}\sqrt{3}\sin\left(-\frac{1}{4}k + \frac{1}{4}l\sqrt{3}\right) - \frac{1}{10}\sqrt{3}\sin\left(\frac{3}{4}k + \frac{1}{4}l\sqrt{3}\right) & -\frac{1}{5}\sqrt{3}\sin(k) - \frac{1}{10}\sqrt{3}\sin\left(\frac{1}{2}k + \frac{1}{2}l\sqrt{3}\right) - \frac{1}{10}\sqrt{3}\sin\left(\frac{1}{2}k - \frac{1}{2}l\sqrt{3}\right) \end{pmatrix},$$

$$P_2 = \begin{pmatrix} 0 & \frac{6}{5}\sin\left(-\frac{1}{4}k + \frac{1}{4}l\sqrt{3}\right) \\ \frac{6}{5}\sin\left(-\frac{1}{4}k + \frac{1}{4}l\sqrt{3}\right) & 0 \end{pmatrix},$$

$$Q_2 = \begin{pmatrix} \frac{6}{5}\sin\left(\frac{1}{4}k + \frac{1}{4}l\sqrt{3}\right) & 0 \\ -\frac{1}{5}\sin\left(\frac{1}{2}l\sqrt{3}\right) & -\frac{1}{10}\sin\left(-\frac{3}{4}k + \frac{1}{4}l\sqrt{3}\right) + \frac{9}{10}\sin\left(\frac{1}{4}k + \frac{1}{4}l\sqrt{3}\right) \end{pmatrix} \quad \text{and}$$

$$R_2 = \begin{pmatrix} 0 & -\frac{1}{10}\sin\left(\frac{3}{4}k + \frac{1}{4}l\sqrt{3}\right) + \frac{9}{10}\sin\left(-\frac{1}{4}k + \frac{1}{4}l\sqrt{3}\right) \\ -\frac{1}{10}\sin\left(\frac{3}{4}k + \frac{1}{4}l\sqrt{3}\right) + \frac{9}{10}\sin\left(-\frac{1}{4}k + \frac{1}{4}l\sqrt{3}\right) & -\frac{3}{10}\sin\left(\frac{1}{2}k + \frac{1}{2}l\sqrt{3}\right) - \frac{3}{20}\sin\left(-\frac{1}{2}k + \frac{1}{2}l\sqrt{3}\right) + \frac{3}{20}\sin\left(\frac{1}{2}k - \frac{1}{2}l\sqrt{3}\right) \end{pmatrix}.$$

The eigenvalues can then be obtained using the method used for the inertia-gravity waves i.e. by finding the eigenvalues of the matrix for various $\boldsymbol{k}\Delta x$ and plotting contours in $\boldsymbol{k}$ space. There is an extra difficulty in the Rossby case, because the numerical algorithm for obtaining eigenvalues of the 4×4 matrix does not preserve the order of the branches when $\boldsymbol{k}\Delta x$ is varied. It is not possible to distinguish the branches by sorting the eigenvalues in numerical order for each $\boldsymbol{k}$ because the branches have values which cross. However, the branches can be distinguished by examining the corresponding eigenvectors. If we interpolate the continuous Fourier modes to the reference hexagon, we obtain four types of solution (after normalisation) for $\tilde{\boldsymbol{\eta}}$, namely

$$\begin{pmatrix} \frac{1}{4} \\ \frac{1}{4} \\ \frac{1}{4} \\ \frac{1}{4} \end{pmatrix}, \quad \begin{pmatrix} \frac{-1}{4} \\ \frac{-1}{4} \\ \frac{1}{4} \\ \frac{1}{4} \end{pmatrix}, \quad \begin{pmatrix} \frac{1}{4} \\ \frac{-1}{4} \\ \frac{-1}{4} \\ \frac{1}{4} \end{pmatrix}, \quad \begin{pmatrix} \frac{-1}{4} \\ \frac{1}{4} \\ \frac{-1}{4} \\ \frac{1}{4} \end{pmatrix},$$

where the fundamental modes take the form of the vector on the left, and higher modes arise from the other three vectors. Hence, we identified the various branches by inspecting the eigenvectors and associating them with the branch which has the same sign pattern as the vectors above.

Fig. 4 shows contour plots of the frequency ω for the case $\hat{\boldsymbol{f}} = (0, 1)$, with parameter values taken from Thuburn [19]. Exactly as the f-plane case, we obtain four roots for ω which correspond to the fundamental modes (i.e. the modes that are possible to represent on a $P1$ mesh) and the higher modes which arise from the extra accuracy on a $P2$ mesh. All the modes correspond to physical values after correct interpretation through the Brillouin zones as for the inertia–gravity wave case. A comparison with the exact dispersion relation for Rossby waves is given in Fig. 5; a very close match is observed. Fig. 6 shows contour plots for the same parameter values but with $\hat{\boldsymbol{f}} = (1, 0)$. Fig. 7 shows the corresponding comparison with the exact

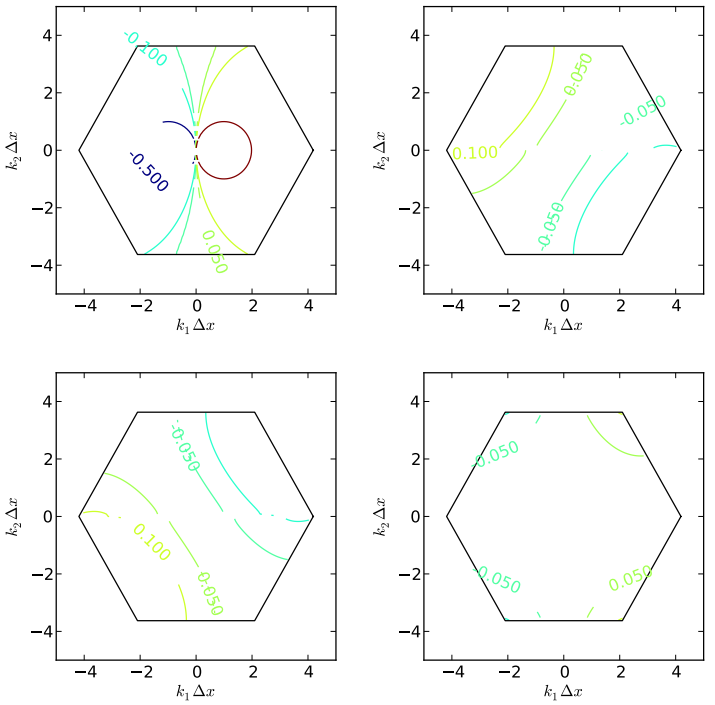

Fig. 4. Contour plots showing $\omega \times 10^6$ obtained from the solutions of Eq. (27), with parameters $f_0 = 1.0 \times 10^{-4}$, $\beta = 1.0 \times 10^{-12}$, $\Delta x = 1.0 \times 10^5$ and $c^2 = 1.0 \times 10^5$ (these parameters are the same as those used in Thuburn [19]). f increases in the y-direction relative to the mesh. The lowest branch of the dispersion relation is shown top-left. The other branches are aliased higher values of $\boldsymbol{k}\Delta x$.

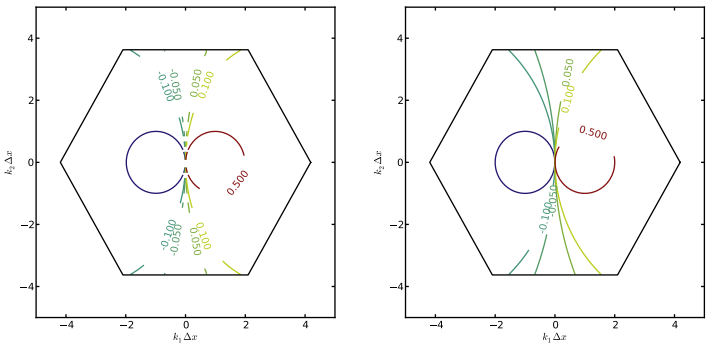

Fig. 5. Comparison between the lowest branch of the discrete dispersion relation (left) and the exact dispersion relation (right). f increases in the y-direction relative to the mesh.

dispersion relation; a close match is again observed. This shows that the $P1_{DG}$–$P2$ discretisation has Rossby waves whose speed is almost independent of the mesh orientation.

5. Summary and outlook

In this paper we analysed the $P1_{DG}$–$P2$ finite element pair applied to the rotating shallow-water equations, by means of a discrete Helmholtz decomposition which exists because of the embedding properties of $P1_{DG}$–$P2$, namely gradients and skew gradients of $P2$ map into $P1_{DG}$. The discrete Helmholtz decomposition has some extra components, which we refer to as spurious velocity components, and which can be projected out, resulting in a discretisation that we referred to as $H(P2)$–$P2$. This decomposition was then used to show that in the f-plane, all steady states are geostrophically balanced (and *vice versa*). Furthermore, a discrete inertia-gravity wave equation can be derived which is the same as the $P2$ continuous finite element method applied to the inertia–gravity wave equation, and hence the inertia–gravity wave solutions are third-order accurate. This should mean that the $P1_{DG}$–$P2$ method should give very stable and accurate solutions of the linear geostrophic adjustment problem. We also showed that the spurious velocity components are uncoupled from the geostrophic balance or

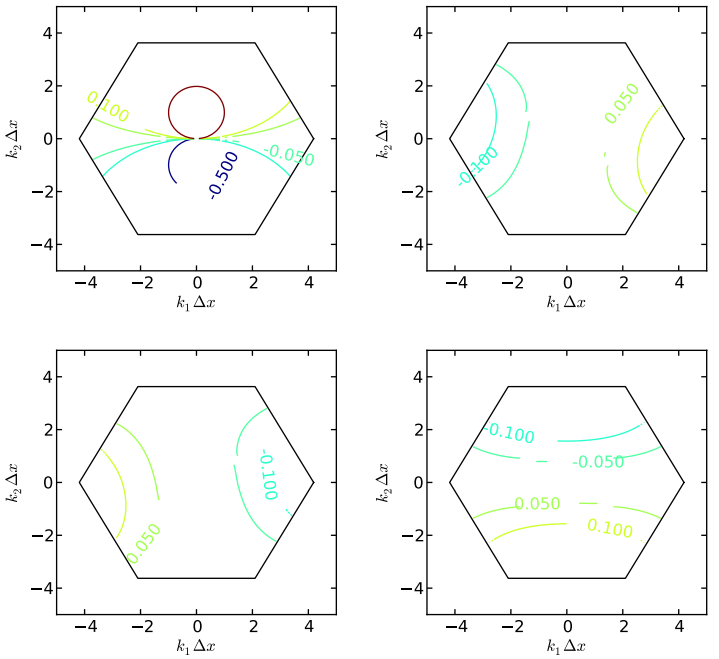

Fig. 6. Contour plots showing $\omega \times 10^6$ obtained from the solutions of Eq. (27), with parameters $f_0 = 1.0 \times 10^{-4}$, $\beta = 1.0 \times 10^{-12}$, $\Delta x = 1.0 \times 10^5$ and $c^2 = 1.0 \times 10^5$ (these parameters are the same as those used in Thuburn [19]). f increases in the x-direction relative to the mesh. The lowest branch of the dispersion relation is shown top-left. The other branches are aliased higher values of $\boldsymbol{k}\Delta x$.

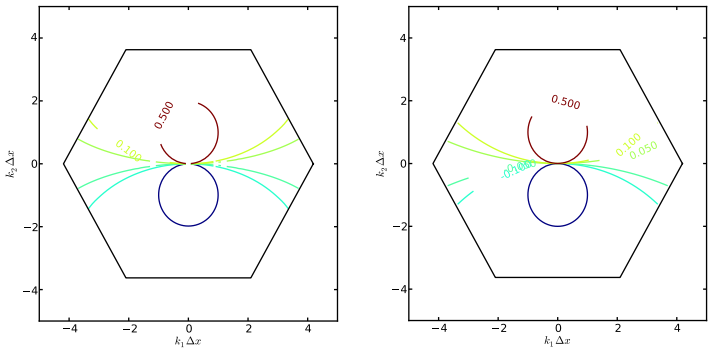

Fig. 7. Comparison between the lowest branch of the discrete dispersion relation (left) and the exact dispersion relation (right). f increases in the x-direction relative to the mesh.

inertia–gravity waves, and they just undergo spurious inertial oscillations which do not propagate. When the $H(P2)$–$P2$ method is used, we obtain identical equations but without the spurious inertial oscillations. The $H(P2)$–$P2$ method may be thought of as an implementation of the $P2$ finite element version of the Z-grid, in which vorticity, streamfunction and layer thickness are all collocated. Hence, the $P1_{DG}$–$P2$ method may be thought of as a way to embed the finite element Z-grid into a method which avoids the need to solve elliptic problems for the potential and streamfunction, at the cost of adding spurious inertial oscillations.

We then followed the methodology of Roux and Pouliot [15], and Thuburn [19], to analyse the Rossby wave equation obtained from the $P1_{DG}$–$P2$ discretisation of the shallow-water equations on the β-plane in the quasi-geostrophic limit. It was shown that the spurious velocity components do not couple in to the Rossby wave dynamics, in fact the geostrophic spurious components vanish and the ageostrophic components are slaved to the geostrophic streamfunction. It was shown that the quasi-geostrophic limit leads to a discrete Rossby wave equation which is identical to the continuous $P2$ finite element discretisation applied to the continuous Rossby wave equation, and hence the $P1_{DG}$–$P2$ Rossby waves are third-order accurate. We expect that this means that the $P1_{DG}$–$P2$ dispersion relation is much more independent of the direction of mesh alignment than other methods with linear velocity (such as the lowest-order Ravier–Thomas element which is the finite element version of the C-grid finite difference method). One seemingly negative aspect of using continuous finite element methods

for pressure is that the mass matrix is not diagonal, so a linear system must be solved even when explicit timestepping is used. On the one hand, solving this linear system iteratively is extremely cheap since the condition number is independent of resolution and hence the number of iterations required stays constant under mesh refinement [7]. On the other hand, one can approximate the mass matrix M by a "lumped" diagonal mass matrix M_L with $(M_L)_{ii} = \sum_j M_{ij}$. It was shown in [9] that lumping the mass has minimal effect on the dispersion relations so we would expect similar properties. In particular note that mass-lumping only affects the time-derivative terms so geostrophic states will remain steady.

It seems almost inevitable (because of the difficulty in balancing the number of velocity and pressure degrees of freedom) that any numerical discretisation that is not based on quadrilateral meshes will result in some form of spurious modes. From the results of this paper it appears that the $P1_{DG}$–$P2$ method puts the spurious modes into the least harmful place: it has no spurious pressure modes which would quickly pollute the solution and result in sub-optimal numerical convergence, it has no spurious Rossby modes which could modify the transfer of energy from barotropic to baroclinic modes in the presence of baroclinic instability, but it does have spurious inertial oscillations which do not propagate, and which can be filtered out using the $H(P2)$–$P2$ projection. Whether or not these modes cause problems depends on how they are coupled to the physical modes through nonlinear advection, and this needs to be studied in careful benchmarks before recommending the $P1_{DG}$–$P2$ method for use in NWP. If the modes are not harmful then the other properties discussed here (super-accurate wave propagation and representation of geostrophic balance on arbitrary unstructured meshes) mean that $P1_{DG}$–$P2$ should be an ideal choice for NWP models using adaptive mesh refinement. Here the projection filter will prove very useful, since the spurious modes can easily be extracted and measured, and modified advection schemes can be proposed which apply the projection before the wave step in semi-implicit splitting methods.

Acknowledgements

This paper began after interesting discussions on spurious modes with Andrew Staniforth, John Thuburn and Nigel Wood.

Appendix A. Supplementary data

Supplementary data associated with this article can be found, in the online version, at doi:10.1016/j.jcp.2010.12.024.

References

[1] A. Arakawa, V. Lamb, Computational design of the basic dynamical processes of the UCLA general circulation model, in: J. Chang (Ed.), Methods in Computational Physics, vol. 17, Academic Press, 1977, pp. 173–265.
[2] S. Brenner, R. Scott, The Mathematical Theory of Finite Element Methods, Springer-Verlag, 1994.
[3] R. Comblen, J. Lambrechts, J.-F. Remacle, V. Legat, Practical evaluation of five partly discontinuous finite element pairs for the non-conservative shallow water equations, Int. J. Numer. Meth. Fluid. 63 (6) (2010) 701–724.
[4] C.J. Cotter, D.A. Ham, C.C. Pain, A mixed discontinuous/continuous finite element pair for shallow-water ocean modelling, Ocean Model. 26 (2009) 86–90.
[5] C.J. Cotter, D.A. Ham, C.C. Pain, S. Reich, LBB stability of a mixed finite element pair for fluid flow simulations, J. Comput. Phys. 228 (3) (2009) 336–348.
[6] M. Fox-Rabinovitz, Computational dispersion properties of 3D staggered grids for a nonhydrostatic anelastic system, Mon. Weather Rev. 124 (1996) 498–510.
[7] P.M. Gresho, R.L. Sani, Incompressible Flow and the Finite Element Method, Isothermal Laminar Flow, vol. 2, Wiley, 2000.
[8] A.M. Kossevich, Geometry of Crystal Lattices, Wiley, 2005.
[9] D. Le Roux, E. Hanert, V. Rostand, B. Pouliot, Impact of mass lumping on gravity and Rossby waves in 2D finite-element shallow-water models, Int. J. Numer. Meth. Fluid 59 (7) (2008) 767–790.
[10] D. Le Roux, A. Staniforth, C.A. Lin, Finite elements for shallow-water equation ocean models, Mon. Weather Rev. 126 (7) (1998) 1931–1951.
[11] D. Majewski, D. Liermann, P. Prohl, B. Ritter, M. Buchhold, T. Hanisch, G. Paul, W. Wergen, J. Baumgardner, The operational global icosahedral-hexagonal gridpoint model GME: description and high-resolution tests, Mon. Weather Rev. 130 (2002) 319–338.
[12] D. Randall, Geostrophic adjustment and the finite-difference shallow-water equations, Mon. Weather Rev. 122 (1994) 1371–1377.
[13] Thomas Raviart, A mixed finite element method for 2nd order elliptic problems, in: Mathematical Aspects of the Finite Element Method. Lecture Notes in Mathematics, Springer, Berlin, 1977, pp. 292–315.
[14] T.D. Ringler, R. Heikes, D. Randall, Modeling the atmospheric general circulation using a spherical geodesic grid: a new class of dynamical cores, Mon. Weather Rev. 128 (2000) 2471–2490.
[15] D.Y.L. Roux, B. Pouliot, Analysis of numerically induced oscillations in two-dimensional finite-element shallow-water models part II: free planetary waves, SIAM J. Sci. Comput. 30 (4) (2008) 1971–1991.
[16] D.Y.L. Roux, V. Rostand, B. Pouliot, Analysis of numerically induced oscillations in 2d finite-element shallow-water models part I: inertia-gravity waves, SIAM J. Sci. Comput. 29 (1) (2007) 331–360.
[17] M. Satoh, T. Matsuno, H. Tomita, H. Miura, T. Nasuno, S. Iga, Nonhydrostatic icosahedral atmospheric model (NICAM) for global cloud resolving simulations, J. Comput. Phys. 227 (7) (2008) 3486–3514.
[18] SymPy Development Team, SymPy: Python library for symbolic mathematics, 2009. <http://www.sympy.org>.
[19] J. Thuburn, Numerical wave propagation on the hexagonal C-grid, J. Comput. Phys. 227 (11) (2008) 5836–5858.
[20] J. Thuburn, T.D. Ringler, W.C. Skamarock, J.B. Klemp, Numerical representation of geostrophic modes on arbitrarily structured C-grids, J. Comput. Phys. 228 (2009) 8321–8335.
[21] G. Umgiesser, D.M. Canu, A. Cucco, C. Solidoro, A finite element model for the Venice Lagoon. Development, set up, calibration and validation, J. Marine Syst. 51 (1-4) (2004) 123–145.
[22] R. Walters, V. Casulli, A robust, finite element model for hydrostatic surface water flows, Commun. Numer. Methods Eng. 14 (1998) 931–940.